Dalton Transactions

Accepted Manuscript

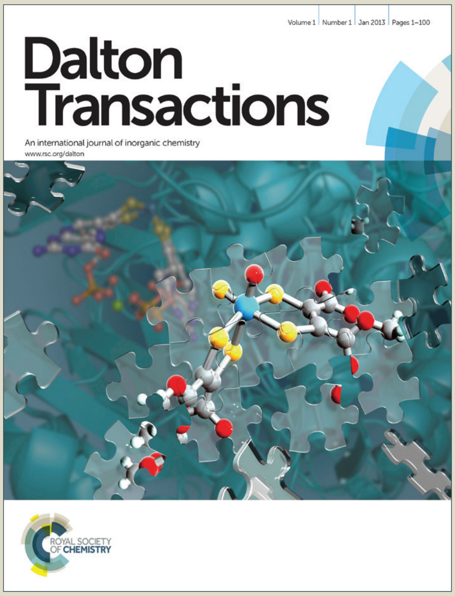

ROYAL SOCIETY OF CHEMISTRY

www.rsc.org/dalton

Dalton Transactions Dynamic Article Links ►

Cite this: DOI: 10.1039/c0xx00000x

www.rsc.org/xxxxxx

ARTICLE TYPE

First Investigation of Synthetic Mechanism and Lithium Intercalation Chemistry of $Li_9Fe_3(P_2O_7)_3(PO_4)_2$/C as Cathode Material for Lithium Ion Batteries

He Gao[a], Sen Zhang*[a] and Chao Deng*[b]

Received (in XXX, XXX) Xth XXXXXXXXX 20XX, Accepted Xth XXXXXXXXX 20XX
DOI: 10.1039/b000000x

Abstract An iron-based mixed-polyanion compound, $Li_9Fe_3(P_2O_7)_3(PO_4)_2$, is introduced as a possible cathode material for Li-ion batteries. Phase-pure $Li_9Fe_3(P_2O_7)_3(PO_4)_2$ is successfully prepared by a sol-gel method, and its physicochemical properties are investigated in detail. Special attention is paid on making clear the variation of the phase composition with the annealing temperature and the effect of carbon coating on the electrochemical performance. Apparently phase-pure $Li_9Fe_3(P_2O_7)_3(PO_4)_2$ can only be obtained in a narrow temperature range, either higher or lower annealing temperature outside this temperature range always leads to impurity phase. The pristine $Li_9Fe_3(P_2O_7)_3(PO_4)_2$ is suffering from its low electronic conductivity (10^{-9} S cm^{-1}) and theoretical capacity (85 mAh·g^{-1}), it has a first discharge capacity of only 36 mAh·g^{-1}. Carbon coating is employed to improve the electrochemical performance. When the carbon content is 10 wt.%, the discharge capacity of $Li_9Fe_3(P_2O_7)_3(PO_4)_2$/C reaches the maximum value of 60 mAh·g^{-1}. The electronic conductivity of the composite, the exact discharge capacity of $Li_9Fe_3(P_2O_7)_3(PO_4)_2$ in the composite and the capacity retention of the composite after 30 cycles vary in the same fashion with an increase in carbon content, i.e. first quickly increase and then stabilize.

Keyword: mixed-polyanion; monodiphosphate; lithium intercalation; carbon coating

1 Introduction

The expanding demand of high-power and high-energy batteries for large-scale applications has motivated the continuous research on materials for lithium ion batteries (LIBs)[1-3]. Polyanion materials are considered promising cathode materials for large-scale LIBs because of its low cost and high safety. Especially, the polyanion materials using earth-abundant iron as the redox center have attracted more and more attention. Iron-based polyanion materials such as Li_2FeSiO_4[4-8], $Li_2FeP_2O_7$[9-12], $LiFeBO_3$[13], $LiFePO_4$[14-16], $Li_3Fe_2(PO_4)_3$[17-19], $LiFeP_2O_7$[17,21-20], etc. have been studied as cathode materials for lithium batteries. Olivine $LiFePO_4$ is considered as one of the most promising cathode materials for large-scale lithium ion batteries.

Mixed-polyanion compounds such as $LiFe_2(SO_4)_2(PO_4)$[22], $A_xM(YO_3)(XO_4)$ (A=Na, Li; X=Si, As, P; Y=C, B; M=a redox active metal; and x=0~3)[23,24], $Li_9M_3(P_2O_7)_3(PO_4)_2$ (M=V, Fe, Mo)[25-27] and $Li_xNa_{4-x}Fe_3(PO_4)_2(P_2O_7)$ (x=0~3)[28] have two kinds of polyanion. Some of them show fascinating physicochemical characteristics as cathode materials for lithium batteries. $Li_9V_3(P_2O_7)_3(PO_4)_2$ [26] has an electronic conductivity of 1.43×10^{-8} S·cm^{-1}, its phosphorus and oxygen deficient form, i.e. $Li_9V_3P_{8-\delta}O_{29-\delta'}$ [29], has a discharge capacity as high as 250 mAh·g^{-1}. The $Li_xNa_{4-x}Fe_3(PO_4)_2(P_2O_7)$ compounds are revealed by first principle calculations as fast ionic conductors, and they can reversibly exchange one electron per Fe atom in both Li and Na cells[28]. Recently, we reported a series of mixed-polyanion materials, i.e. $Li_{2+x}Fe_{1-x}P_xSi_{1-x}O_4$/C[30], $Li_{1-x}Fe_{1+x}P_{1-x}Si_xO_4$/C[31] and $Li_{2+x}Mn_{1-x}P_xSi_{1-x}O_4$/C[32]. Some of them show desirable electrochemical performance. The rich chemistry of the mixed-polyanion compounds will enable us to develop a growing number of new cathode materials for lithium batteries in the future.

Two kinds of polyanion, i.e. $(PO_4)^{3-}$ and $(P_2O_7)^{4-}$, coexist in $Li_9Fe_3(P_2O_7)_3(PO_4)_2$ which employs earth-abundant iron as the redox center. Its crystal structure was first described by Poisson et al. in 1998[25], and it was not until 2010 that it found its application as a photocatalyst working under visible light[33]. Until now, there is no report on its application as a cathode material for lithium battery. In this study, we prepared $Li_9Fe_3(P_2O_7)_3(PO_4)_2$ by a sol-gel method and subsequently characterized its physicochemical behavior. Special attention is focused on the synthetic optimization, structural analysis, lithium intercalation and carbon coating. The results will not only provide a possible view on designing new materials for lithium ion batteries, but also enrich the knowledge on mixed-polyanion materials.

2 Experimental

2.1 Synthesis.

$Li_9Fe_3(P_2O_7)_3(PO_4)_2$ was prepared by a sol-gel method. Stoichiometric amount of analytical reagents, lithium acetate, ammonium dihydrogen phosphate, ferric nitrate and citric acid were used as starting materials. All the reagents were dissolved in distilled water, and then the solution was kept at 80 ^oC under magnetic stirring until a wet gel was formed. The resulting wet gel was dried at 100 ^oC over night to form a dry gel. The dry gel was ground and then calcined at a selected temperature for 12 h in air. The selected calcination temperatures are 550, 600, 650, 700, 750, 800 and 850 ^oC, respectively. The $Li_9Fe_3(P_2O_7)_3(PO_4)_2/C$ composites were prepared by ball-milling the pristine $Li_9Fe_3(P_2O_7)_3(PO_4)_2$ with different amount of carbon for 10 hours.

2.2 Materials characterization

Powder X-ray diffraction (XRD, Bruker D8/Germany) using Cu Kα radiation was employed to identify the crystalline phase of the material. The experiment was performed by using step mode with a fixed time of 3 s and a step size of 0.02^o. The morphology was observed with a scanning electron microscope (SEM, HITACHI S-4700) and a transmission electron microscope (TEM, JEOS-2010 PHILIPS), and the chemical composition was determined by an energy dispersive X-ray detector (EDX) coupled with the SEM. The weight loss and the heat flow upon temperature ramping were monitored by thermogravimetry and differential scanning calorimetry (TG/DSC, NETZSCH STA 449C), respectively. A vibrating sample magnetometer (VSM) was used to identify the magnetic behavior of the material. The electronic conductivity was measured by the four-probe technique. The powder was pressed into a disk with a diameter of 20 mm and a thickness of about 0.9 mm at a pressure of 10 MPa, and the disk was annealed at 750 ^oC for 2 hour in air. Gold was painted on both sides of the disk to ensure electrical contact. The ^{57}Fe Mössbauer spectrum was recorded in transmission mode at room temperature on an MS-500 constant accelerator spectrometer using a $^{57}Co/Pd$ source. The isomer shift was given relative to the center of α-Fe. The experimental spectrum was fitted to Lorentzian lines by using a least-squares-based method.

2.3 Electrochemical measurements

The coin cells were prepared as described in Ref.[34]. The composite electrode was made from a mixture of the prepared sample, acetylene black, and Polyvinylidene Fluoride in a weight ratio of 80:10:10. A disk of fresh lithium foil was used as counter electrode. The 1 mol·L^{-1} $LiPF_6$ dissolved in a mixture of ethylene carbonate (EC) and diethyl carbonate (DEC) was used as the electrolyte. Galvanostatic charge-discharge measurements were performed in a potential range of 1.5~4.8 V vs. Li/Li$^+$ at ambient temperature on a Land battery testing system (Wuhan, China). In the galvanostatic intermittent titration technique (GITT), a constant current of 1/30 C was applied for 10 min and then it was interrupted to achieve open circuit condition for 40 min. This process was repeated until the electrode potential reached the cut-off voltage.

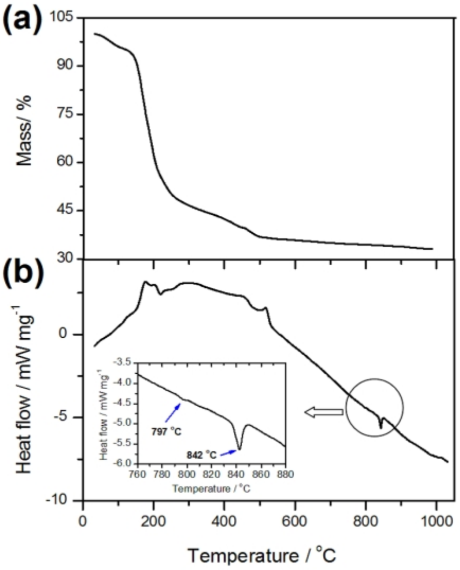

Figure 1 TG (a) and DSC (b) curves of the gel precursor.

3 Results and Discussion

3.1 Variation of phase composition with annealing temperature

In this study, a simple sol-gel method was used to prepare $Li_9Fe_3(P_2O_7)_3(PO_4)_2$, and the dry gel was finally annealed to get the final product. In order to select a suitable annealing temperature, TG and DSC curves were recorded to monitor the weight loss and the heat flow of the dry gel, and the results are shown in Figure 1 (a) and (b), respectively. The TG curve can be divided into four regions. Weight losses of 6%, 39%, 20% and 3% are observed in the temperature ranges of 33~138 ^oC, 138~218 ^oC, 218~518 ^oC and 518~1000 ^oC, respectively. Weakly bonded water was evaporated in the first region. The exothermic peak in the second region can be attributed to the evaporation of strongly bonded water and the pyrolysis of organic species. The broad exothermic peak in the third region can be ascribed to the combustion of residual organic species. Finally, different phases were crystallized in the fourth region. Therefore, the annealing temperatures should be selected in the fourth region. However, as shown in the inset of Figure 1(b), there is an endothermic peak at 842 ^oC with a minor satellite at 797 ^oC, which suggests the formation of other phases. In order to clarify how the phase composition varies with the annealing temperature, a series of temperatures ranging from 550 to 850 ^oC with an interval of 50 ^oC was selected.

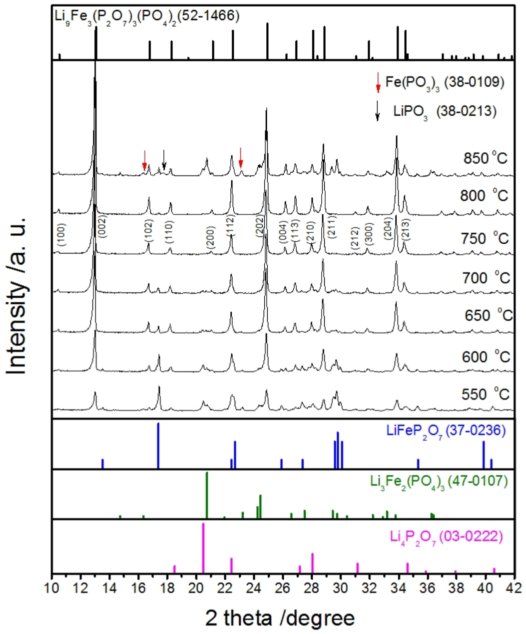

Figure 2 XRD patterns of the samples annealed at different temperature.

The XRD patterns of the samples annealed at different temperatures are shown in Figure 2. Three impurity phases, i.e. $LiFeP_2O_7$, $Li_3Fe_2(PO_4)_3$ and $Li_4P_2O_7$, coexist with the $Li_9Fe_3(P_2O_7)_3(PO_4)_2$ phase in the sample annealed at 550 ^oC which has a light pink color. The intensities of the impurity peaks diminish with increasing annealing temperature until 750 ^oC, and the color of the sample changes accordingly. When the annealing temperature is 750 ^oC, the disappearance of the impurities results in the phase-pure $Li_9Fe_3(P_2O_7)_3(PO_4)_2$ with a light gray color. Therefore, the three impurities can react with each other to form $Li_9Fe_3(P_2O_7)_3(PO_4)_2$ (Equation 1).

$$\mathbf{2Li_3Fe_2(PO_4)_3 + 4Li_4P_2O_7 + 5LiFeP_2O_7 \rightarrow 3Li_9Fe_3(P_2O_7)_3(PO_4)_2} \quad (1)$$

However, a tiny peak of $LiFeP_2O_7$ appeared again in the XRD pattern when the annealing temperature was further increased to 800 ^oC. The three former impurities, i.e. $LiFeP_2O_7$, $Li_3Fe_2(PO_4)_3$ and $Li_4P_2O_7$, reappear when the annealing temperature is 850 ^oC. That is to say, $Li_9Fe_3(P_2O_7)_3(PO_4)_2$ decomposes along the opposite direction of Equation 1 (Equation 2). Additional peaks centered at 16.38^o, 17.82^o and 23.1^o, which can be ascribed to $Fe(PO_3)_3$ and $LiPO_3$ (Equation 3 and 4), are barely observed in the XRD pattern of the purplish sample annealed at 850 ^oC. The reappearance of $LiFeP_2O_7$ at 800 ^oC and the extensive decomposition products at 850 ^oC are in accord with the minor endothermic peak at 797 ^oC and the significant endothermic peak at 842 ^oC, respectively.

$$\mathbf{3Li_9Fe_3(P_2O_7)_3(PO_4)_2 \rightarrow 2Li_3Fe_2(PO_4)_3 + 4Li_4P_2O_7 + 5LiFeP_2O_7} \quad (2)$$

$$\mathbf{3LiFeP_2O_7 \rightarrow Li_3Fe_2(PO_4)_3 + Fe(PO_3)_3} \quad (3)$$

$$\mathbf{Li_4P_2O_7 \rightarrow Li_3PO_4 + LiPO_3} \quad (4)$$

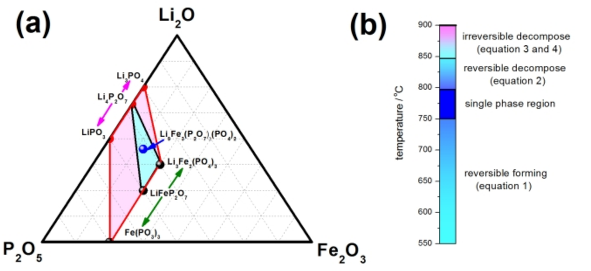

Figure 3 Li_2O-Fe_2O_3-P_2O_5 ternary phase diagram (a) and schematic diagram (b) for the variation of phase composition with annealing temperature.

All of the compounds included in Equations 1-4 are pictured in the ternary phase diagram (Li_2O-Fe_2O_3-P_2O_5) to directly show the relationship between them. They are identified from the XRD patterns of the samples annealed at various temperatures. The ternary phase diagram is of great help to make clear the reaction involved in the annealing process. As displayed in Figure 3(a), $Li_9Fe_3(P_2O_7)_3(PO_4)_2$ lies in the interior of the triangle with $LiFeP_2O_7$, $Li_3Fe_2(PO_4)_3$ and $Li_4P_2O_7$ as vertexes, which can give a reasonable explanation to the formation and decomposition reactions (Equation 1 and 2). The further decomposition reactions of $LiFeP_2O_7$ and $Li_4P_2O_7$ (Equation 3 and 4), which is parallel to each other in the phase diagram, enlarge the triangle into a trapezoid. All the impurities lie on the edge of the trapezoid. Special attention should be paid on $Li_3Fe_2(PO_4)_3$ which is the only common vertex of the triangle and the trapezoid. Therefore, $Li_3Fe_2(PO_4)_3$ does not decompose until the upper limit of the annealing temperature in this study, which is consistent with its ease of preparation in a wide temperature range. The ternary phase diagram clearly shows the relationship between the $Li_9Fe_3(P_2O_7)_3(PO_4)_2$ phase and the impurity phases. As schematically displayed in Figure 3(b), single-phase $Li_9Fe_3(P_2O_7)_3(PO_4)_2$ can only be obtained in a narrow annealing-temperature range.

3.2 Physical characteristics of $Li_9Fe_3(P_2O_7)_3(PO_4)_2$

Further physicochemical characterizations were carried out on the single phase $Li_9Fe_3(P_2O_7)_3(PO_4)_2$. Its XRD pattern can be indexed on the basis of the $P\bar{3}c1$ space group (165) in the trigonal crystal system. The Rietveld refinement was carried out by Maud, and the results are shown in Figure 4(a). The lattice parameters are a=9.7335(3) Å, c=13.6203(2) Å and V=1117.5(5) Å^3. The TEM images of $Li_9Fe_3(P_2O_7)_3(PO_4)_2$ are shown in Figure 4(b). The secondary micron particle consists of primary submicron particles. It is well known that larger particles lead to longer diffusion pathway upon lithium de/intercalation, which is detrimental to the high-rate capability. The particles of $Li_9Fe_3(P_2O_7)_3(PO_4)_2$ are too large to facilitate lithium de/intercalation. Electronic conductivity is another important factor which has profound effect on the electrochemical performance. The current-voltage response of the disk was recorded in Figure 5(a). A linear fit of the current-voltage

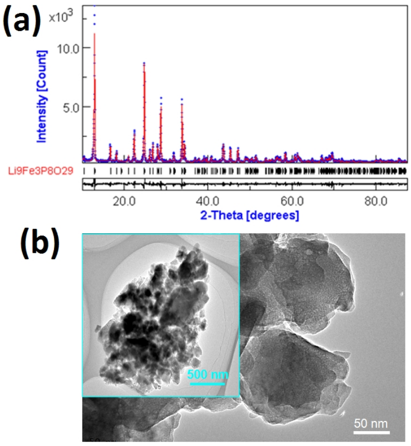

Figure 4 (a) Rietveld refinement of the XRD pattern, R_w=8.08%, R_{wp}=10.16%. (b) TEM images of $Li_9Fe_3(P_2O_7)_3(PO_4)_2$.

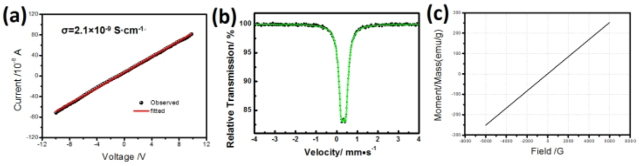

Figure 5 Physical characteristics of $Li_9Fe_3(P_2O_7)_3(PO_4)_2$: (a) current-voltage response for the determination of electronic conductivity; (b) ^{57}Fe mössbauer spectrum; (c) magnetic behavior.

response results in the electronic conductivity of 2.1×10^{-9} S·cm^{-1} at ambient temperature which is in the same order of magnitude as that of $LiFePO_4$ (~10^{-9} S·cm^{-1})[35]. The electronic conductivity is too low to be desirable for good electrochemical performance, especially at high current density. ^{57}Fe Mössbauer spectroscopy was employed to tell the oxidation state of Fe, the resulting spectrum is displayed in Figure 5(b). The spectrum is characterized by a doublet signal including an isomer shift of 0.41 mm·s^{-1} and a quadrupole splitting of 0.21 mm·s^{-1}. The isomer shift of ~0.4 mm·s^{-1} is characteristic of high-spin octahedrally coordinated Fe^{3+}.[36] The magnetic behavior is evaluated by recording magnetization over a range of field at room temperature (Figure 5(c)). The magnetization of $Li_9Fe_3(P_2O_7)_3(PO_4)_2$ shows a linear behavior without hysteresis, indicating the antiferromagnetic character of the ordered Fe^{3+} state[37]. The lack of ferromagnetic interaction indicates the absence of different valence state, which is in accordance with the result of ^{57}Fe Mössbauer spectroscopy.

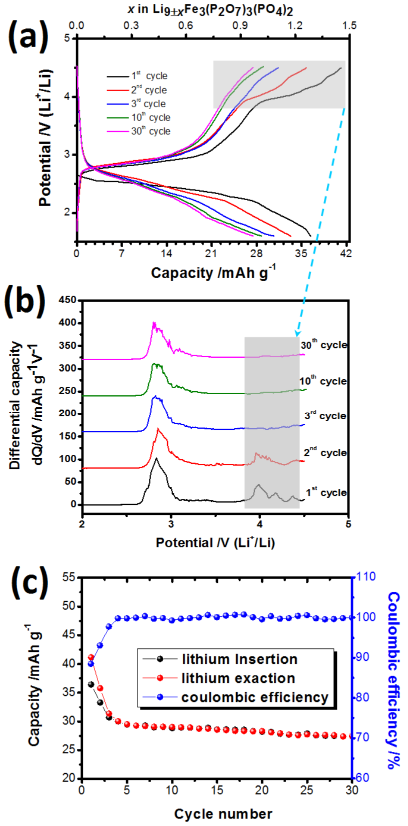

Figure 6 Electrochemical performance of $Li_9Fe_3(P_2O_7)_3(PO_4)_2$ at ambient temperature: (a) galvanostatic discharge/charge curves; (b) differential capacity vs. potential curves of the shaded part of (a); (c) cycling performance.

3.3 Electrochemical characteristics of $Li_9Fe_3(P_2O_7)_3(PO_4)_2$

We carried out the galvanostatic charge/discharge measurements on the prepared $Li_9Fe_3(P_2O_7)_3(PO_4)_2$ at ambient temperature. The applied voltage range and current density are 4.5~1.8 V (vs. Li/Li^+) and C/15 (5 h per Li), respectively. The theoretical capacity of $Li_9Fe_3(P_2O_7)_3(PO_4)_2$ is 85 mAh·g^{-1}. About 36 mAh·g^{-1} (1.3 Li per formula unit) is inserted into the crystal structure of $Li_9Fe_3(P_2O_7)_3(PO_4)_2$ in the first discharge (Figure 6(a)). And more lithium (about 1.45 Li per formula unit) is extracted in the following charging process, attaining a charge capacity of 41 mAh·g^{-1}. In order to better understand the galvanostatic charge curves, they (Figure 6(a)) are differentiated to obtain the corresponding differential capacity vs. potential curves (Figure 6(b)). The peaks in the differential capacity vs. potential curve usually correspond to the potential plateaus in the galvanostatic charge curve. The differential capacity vs. potential curve of the first charge has a major peak at 2.83 V and three minor peaks at 4.0 V, 4.18 V and 4.39 V. The three minor peaks (Figure 6(b)) quickly fade upon cycling and finally disappear in the third charge curve. The cycling performance of $Li_9Fe_3(P_2O_7)_3(PO_4)_2$ is shown in Figure 6(c). The charge and discharge capacity decrease, but the coulombic efficiency increases in the initial few cycles. Special attention should be paid on the initial three cycles whose columbic efficiencies are lower than 1.0. Therefore, besides the inserted lithium, more lithium is extracted. The extra extracted lithium might come from the original lithium in the crystal structure. The low capacity and the fast capacity fading of the $Li_9Fe_3(P_2O_7)_3(PO_4)_2$ can be

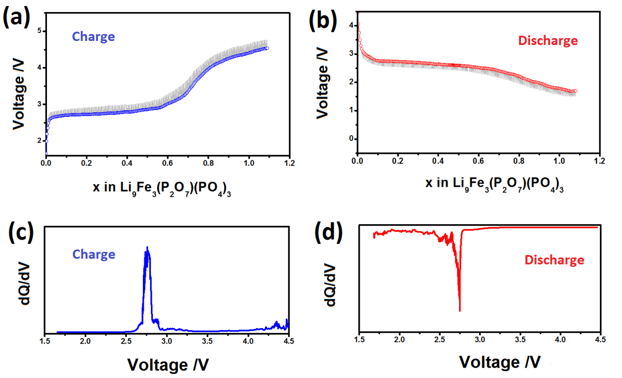

Figure 7 GITT evaluation of $Li_9Fe_3(P_2O_7)_3(PO_4)_2$: GITT charge (a) and discharge (b) curve with emphasis on QOCPs; (c) and (d) differential capacity vs. voltage (dQ/dV) curve on the basis of QOCP curve are displayed as inert.

attributed to its low electronic conductivity. Therefore, Carbon coating can significantly improve the electronic conductivity and the electrochemical property, which is detailed in section 3.4.

The large potential difference between charge and discharge is an indication of high electrode polarization which can be attributed to the large particle size and the low electronic conductivity of $Li_9Fe_3(P_2O_7)_3(PO_4)_2$. In order to clarify the nature of lithium de/intercalation, GITT was employed to obtain the quasi open-circuit potential (QOCP) upon charge and discharge (Figure 7a and b). The QOCP charge/discharge curve is flatter than the galvanostatic charge/discharge curve, and the potential difference between charge and discharge for the QOCP curves is much lower than that for the galvanostatic curves. The lack of fixed-voltage region in the QOCP curves indicates that the lithium de/intercalation reaction might proceed without the coexistence of two phases according to the Gibbs phase rule[12]. Therefore, the de/lithiation reaction might occur via a solid-solution mechanism, which is similar to $Li_2FeP_2O_7$[12].

The QOCP charge/discharge curves are differentiated to obtained the equilibrium redox potential of the Fe^{3+}/Fe^{2+} redox couple in $Li_9Fe_3(P_2O_7)_3(PO_4)_2$ (Figure 7c and d). The equilibrium redox potential is 2.754 V. It is well known that the redox potential of Fe^{3+}/Fe^{2+} in the iron-based polyanion compounds is related to the strength of Fe-O bonds which is affected by the inductive effect of the polyanion. Stronger Fe-O bond is shorter, which leads to lower redox potential. Therefore, the inductive effect of the polyanion has effect on the redox potential of Fe^{3+}/Fe^{2+}. The redox potentials of the Fe^{3+}/Fe^{2+} redox couples in $Li_3Fe_2(PO_4)_3$ and $LiFeP_2O_7$ are already reported[11,17]. Table 1 lists the redox potential of Fe^{3+}/Fe^{2+} and the average length of the Fe-O bond in $Li_9Fe_3(P_2O_7)_3(PO_4)_2$ together with those in $Li_3Fe_2(PO_4)_3$ and $LiFeP_2O_7$. The redox potential of Fe^{3+}/Fe^{2+} in $Li_9Fe_3(P_2O_7)_3(PO_4)_2$ is lower than those in $LiFeP_2O_7$ and $Li_3Fe_2(PO_4)_3$. Although the P/Fe ratio (8:3) in $Li_9Fe_3(P_2O_7)_3(PO_4)_2$ is the highest, its redox potential of Fe^{3+}/Fe^{2+} is the lowest because its average Fe-O bond length is the shortest[21]. Shorter F-O bond is stronger, which leads to lower redox potential of Fe^{3+}/Fe^{2+}.

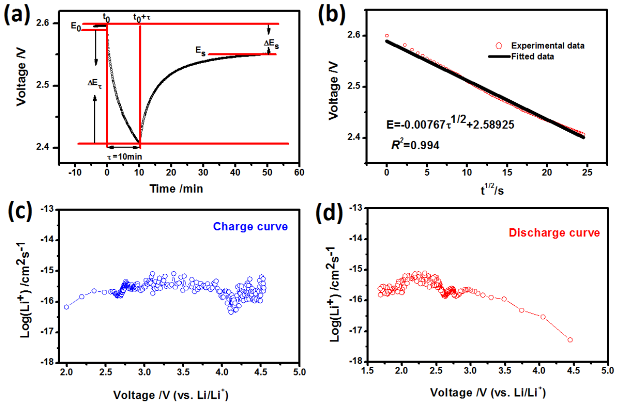

Figure 8 (a) *E* vs. *t* curve of a single titration in GITT. (b) Linear relationship between *E* and $\tau^{1/2}$. (c,d) Variation of the Li^+ diffusion coefficient with the electrode voltage upon (c) charge and (d) discharge.

Furthermore, the Li^+ diffusion coefficients (D_{Li}) were estimated by GITT [38]. According to the Fick's second law of diffusion, D_{Li} can be calculated on the basis of the following equation:

$$D_{Li} = \frac{4}{p}\left(\frac{m_B V_m}{M_B A}\right)^2 \left(\frac{\Delta E_S}{t\left(\frac{dE_t}{d\sqrt{t}}\right)}\right)^2 \quad (\tau<<L^2/D_{Li}) \qquad (5)$$

Where D_{Li} (cm^2s^{-1}) is the Li^+ diffusion coefficient; m_B, M_B and V_m are the mass, molecular weight, molar volume of the electrode material, respectively; A is the interfacial area between electrode and electrolyte; τ is the duration of the current pulse. If the relationship between *E* and $t^{1/2}$ is linear, Equation 5 can be simplified as following [39]:

$$D_{Li} = \frac{4}{pt}\left(\frac{m_B V_m}{M_B A}\right)^2 \left(\frac{\Delta E_S}{\Delta E_t}\right)^2 \qquad (6)$$

In this study, the linear relationship between *E* and $t^{1/2}$ demonstrates the validity of Equation (6) (Figure 8(a),(b)). Figure 8(c) and (d) show the variation of D_{Li} as a function of voltage in the charge and discharge process, respectively. It is shown that the value of D_{Li} varies between 10^{-18} and 10^{-15} cm^2s^{-1}, which is very low. The low Li^+ diffusion coefficients are consistent with the poor electrochemical performance of $Li_9Fe_3(P_2O_7)_3(PO_4)_2$.

3.4 Effect of carbon coating on the properties of $Li_9Fe_3(P_2O_7)_3(PO_4)_2$

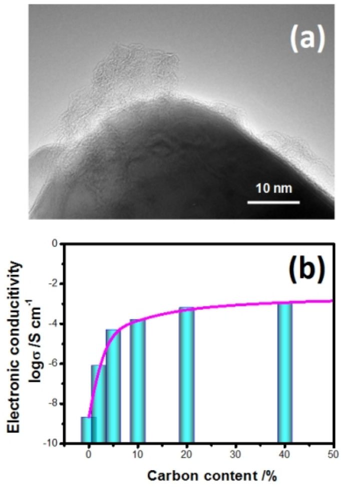

Figure 9 (a) HRTEM image of $Li_9Fe_3(P_2O_7)_3(PO_4)_2$/C with 10 wt.% carbon and (b) variation of the electronic conductivity.

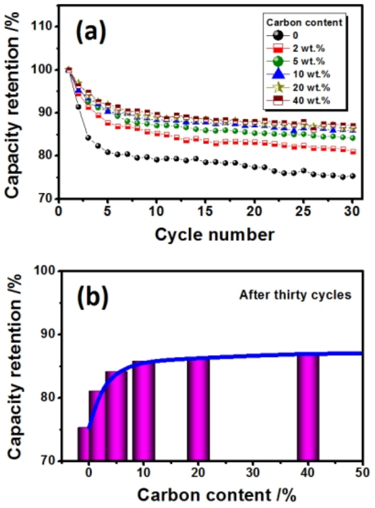

Figure 11 (a) cycle performance and (b) the variation of the capacity retention after 30 cycles with the carbon content.

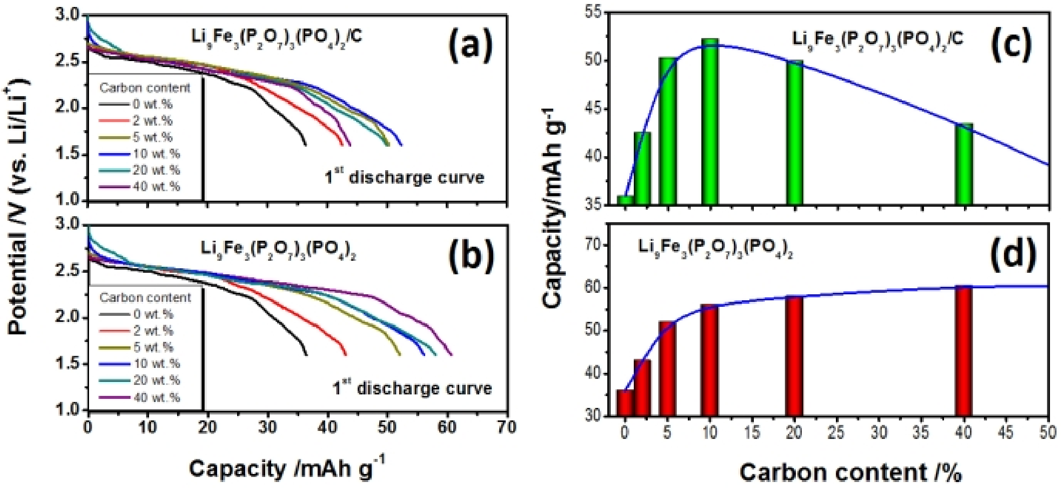

Figure 10 (a) the first discharge curve/capacity (a/c) of $Li_9Fe_3(P_2O_7)_3(PO_4)_2$/C and (b) the exact discharge curve/capacity (b/d) of $Li_9Fe_3(P_2O_7)_3(PO_4)_2$ in the composite with the carbon content.

In order to improve the electrochemical property of $Li_9Fe_3(P_2O_7)_3(PO_4)_2$, carbon coating is employed to modify the pristine materials. The electrochemical performance of pristine $Li_9Fe_3(P_2O_7)_3(PO_4)_2$ is poor because polyanion material usually has a low electronic conductivity. Cabon coating is employed to improve the electronic conductivity, and the carbon content is varied from 2 wt.% to 40 wt.%. Figure 9(a) displays the HRTEM image of the $Li_9Fe_3(P_2O_7)_3(PO_4)_2$/C composite with 10 wt.% carbon. Uneven carbon layer is observed on the surface of the $Li_9Fe_3(P_2O_7)_3(PO_4)_2$ particle. Therefore, ball-milling is not an efficient method for carbon coating, which leads to the poor carbon layer. The electronic conductivity of is obtained when the carbon content is 10 wt.%. The rate of increase is faster than that of decrease. The increase in the discharge capacity can be attributed to the increase in the electronic conductivity, while the decrease can be attributed to the excessive carbon in the composite. In fact, the carbon has a discharge capacity of 18.7 mAh·g^{-1} within the same voltage range in terms of capacitance effect. In order to evaluate the exact discharge capacity of $Li_9Fe_3(P_2O_7)_3(PO_4)_2$ in each composite, the weight and discharge capacity of carbon is excluded and the results are shown in Figure 10(c) and (d). Upon increasing the carbon content, the exact discharge capacity of $Li_9Fe_3(P_2O_7)_3(PO_4)_2$ continuously increases, while its increment declines. It varies in the same fashion as the electronic conductivity, which indicates that the electronic conductivity plays a dominant role in determining the electrochemical performance of $Li_9Fe_3(P_2O_7)_3(PO_4)_2$. Figure 11(a) shows the cycle performance of $Li_9Fe_3(P_2O_7)_3(PO_4)_2$/C, and the inset of Figure 11(b) summarizes the capacity retention after thirty cycles which also varies in the same fashion as the electronic conductivity. A reasonable capacity retention can be obtained when the carbon content is higher than 10 wt.%. In summary, the way in which the electrochemical performance of $Li_9Fe_3(P_2O_7)_3(PO_4)_2$/C varies with the carbon content is a compromise between the electronic conductivity and the excessive carbon. Therefore, the optimal carbon content is 10 wt.%.

4 Conclusions

In this study, the lithium iron monodiphosphate, i.e. $Li_9Fe_3(P_2O_7)_3(PO_4)_2$, was introduced as a possible cathode material for lithium batteries. Special attention is focused on the synthetic optimization, structural analysis, lithium intercalation and carbon coating. Both DSC and XRD results confirm the formation of phase-pure $Li_9Fe_3(P_2O_7)_3(PO_4)_2$ in a narrow annealing-temperature range. However, the discharge capacity of $Li_9Fe_3(P_2O_7)_3(PO_4)_2$ is only 36 $mAh{\cdot}g^{-1}$ because of its poor electronic conductivity (10^{-9} S cm^{-1}) and low theoretical capacity (85 $mAh{\cdot}g^{-1}$). Carbon coating with different carbon content is employed to improve the electrochemical performance of $Li_9Fe_3(P_2O_7)_3(PO_4)_2$. The electronic conductivity of the composite, the exact discharge capacity of $Li_9Fe_3(P_2O_7)_3(PO_4)_2$ in the composite and the capacity retention of the composite after 30 cycles vary in the same fashion with an increase in carbon content, i.e. first quickly increase and then stabilize. Considering the $Li_9Fe_3(P_2O_7)_3(PO_4)_2$/C composite as a whole, the sample with 10 wt.% carbon has the best electrochemical performance, its discharge capacity and capacity retention after thirty cycles are 52 $mAh{\cdot}g^{-1}$ and 86%, respectively.

Acknowledgement

This work is supported by the National Natural Science Foundation of China (No. 21001036, 50902041), Fundamental Research Funds for the Central Universities (HEUCF201310011), Program for New Century Excellent Talents in Heilongjiang Provincial University (No. 1253-NCET-012) and Natural Science Foundation of Heilongjiang Province (No. QC2013C008).

Notes and referencesa

[b]*Key Laboratory of Superlight Material and Surface Technology, Ministry of Education, College of Material Science and Chemical Engineering, Harbin Engineering University, Harbin 150001, Heilongjiang, China; E-Mail: senzhang@hrbeu.edu.cn*

[b]*Key Laboratory for Photonic and Electronic Bandgap Materials, Ministry of Education; College of Chemistry and Chemical Engineering, Harbin Normal University, Harbin, 150025, Heilongjiang, China; E-Mail: chaodenghsd@sina.com*

1 B. Kang, G. Ceder, *Nature* **2009**, *458*, 190.
2 A. Yamada, N. Iwane, Y. Harada, S. Nishimura, Y. Koyama, I. Tanaka, *Adv. Mater.* **2010**, *22*, 3583.
3 C. Deng, S. Zhang, S. Y. Yang, Y. Gao, B. Wu, L. Ma, B. L. Fu, Q. Wu, F. L. Liu, *J. Phys. Chem. C* **2011**, *115*, 15048.
4 A. R. Armstrong, N. Kuganathan, M. S. Islam, P. G. Bruce, *J. Am. Chem. Soc.* **2011**, *133*, 13031.
5 C. Deng, S. Zhang, S. Y. Yang, *Mater. Chem. Phys.* **2010**, *120*, 14.
6 C. Deng, S. Zhang, S. Y. Yang, B. L. Fu, L. Ma, *J. Power Sources* **2011**, *196*, 386.
7 D. Ensling, M. Stjerndahl, A. Nyton, T. Gustafsson, J. O. Thomas, *J. Mater. Chem.* **2009**, *19*, 82.
8 S. Zhang, C. Deng, B. L. Fu, S. Y. Yang, L. Ma, *Electrochim. Acta* **2010**, *55*, 8482.
9 S. I. Nishimura, M. Nakamura, R. Natsui, A. Yamada, *J. Am. Chem. Soc.* **2010**, *132*, 13596.
10 H. Kim, S. Lee, Y. U. Park, H. Kim, J. Kim, S. Jeon, K. Kang, *Chem. Mater.* **2011**, *23*, 3930.
11 N. Furuta, S. I. Nishimura, P. Barpanda, A. Yamada, *Chem. Mater.* **2012**, *24*, 1055.
12 D. Shimizu, S. I. Nishimura, P. Barpanda, A. Yamada, *Chem. Mater.* **2012**, *24*, 2598.
13 Y. Janssen, D. S. Middlemiss, S. H. Bo, C. P. Grey, P. G. Khalifah, *J. Am. Chem. Soc.* **2012**, *134*, 20516.
14 A. K. Padhi, K. S. Nanjundaswamy, J. B. Goodenough, *J. Electrochem. Soc.* **1997**, *144*, 1188.
15 C. A. J. Fisher, M. S. Islam, *J. Mater. Chem.* **2008**, *18*, 1209.
16 A. Vu, A. Stein, *Chem. Mater.* **2011**, *23*, 3237.
17 A. K. Padhi, K. S. Nanjundaswamy, C. Masquelier, S. Okada, J. B. Goodenough, *J. Electrochem. Soc.* **1997**, *144*, 1609.
18 J. Cabana, J. Shirakawa, M. Nakayama, M. Wakihara, C. P. Grey, *J. Mater. Chem.* **2011**, *21*, 10012.
19 A. S. Andersson, B. Kalska, P. Eyob, D. Aernout, L. Haggstrom, J. O. Thomas, *Solid State Ion.* **2001**, *140*, 63.
20 N. Plylahan, C. Vidal-Abarca, P. Lavela, J. L. Tirado, *Electrochim. Acta* **2012**, *62*, 124.
21 C. Wurm, M. Morcrette, G. Rousse, L. Dupont, C. Masquelier, *Chem. Mater.* **2002**, *14*, 2701.
22 A. K. Padhi, V. Manivannan, J. B. Goodenough, *J. Electrochem. Soc.* **1998**, *145*, 1518.
23 G. Hautier, A. Jain, H. Chen, C. Moore, S. P. Ong, G. Ceder, *J. Mater. Chem.* **2011**, *21*, 17147.
24 H. Chen, G. Hautier, A. Jain, C. Moore, B. Kang, R. Doe, L. Wu, Y. Zhu, Y. Tang, G. Ceder, *Chem. Mater.* **2012**, *24*, 2009.
25 S. Poisson, F. D. Yvoire, N. H. Dung, E. Bretey, P. *J. Solid State Chem.* **1998**, *138*, 32.
26 Q. Kuang, Y. M. Zhao, J. T. Xu, *J. Phys. Chem. C* **2011**, *115*, 8422.
27 A. Jain, G. Hautier, C. Moore, B. Kang, J. Lee, H. Chen, N. Twu, G. Ceder, J. *Electrochem. Soc.* **2012**, *159*, A622.
28 H. Kim, I. Park, D. H. Seo, S. Lee, S. W. Kim, W. J. Kwon, Y. U. Park, C. S. Kim, S. Jeon, K. Kang, *J. Am. Chem. Soc.* **2012**, *134*, 10369.
29 M. Onoda, S. Ikeda, T. Ishibashi, *J. Phys.-Condens. Matter* **2012**, *24*, 085402.
30 C. Deng, S. Zhang, G. S. Zhao, Z. Dong, Y. Shang, Y. X. Wu, B. D. Zhao, *J. Electrochem. Soc.* **2013**, *160*, A1457.
31 S. Zhang, C. Deng, H. Gao, F. L. Meng, M. Zhang, *Electrochim. Acta* **2013**, *107*, 406.
32 C. Deng, S. Zhang, Y. H. Sun, Y. Gao, Q. Wu, F. L. Liu, *J. Electrochem. Soc.* **2013**, *160*, A218.

33 F. Ji, C. L. Li, J. H. Zhang, *ACS Appl. Mater. Interfaces* **2010**, *2*, 1674.

34 S. Zhang, Q. Wu, C. Deng, F. L. Liu, M. Zhang, F. L. Meng, H. Gao, *J. Power Sources* **2012**, *218*, 56.

35 P. S. Herle, B. Ellis, N. Coombs, L. F. Narzar, *Nat. Mater.* **2004**, *3*, 147.

36 M. Ren, Z. Zhou, Y. Li, X. P. Gao, J. Yan, *J. Power Sources* **2006**, *162*, 1357.

37 L. Vijayan, R. Chenruku, G. Govindaraj, *J. Appl. Phys.* **2012**, *111*, 064905.

38 W. Weppner, R. A. Huggins, *J. Electrochem. Soc.* **1977**, *124*, 1569.

39 E. Deiss, *Electrochimica Acta* **2005**, *50*, 2927.

Graphic Abstract

First investigation of synthetic mechanism and lithium intercalation chemistry of $Li_9Fe_3(P_2O_7)_3(PO_4)_2$/C as cathode material for lithium ion batteries

H. Gao[1], S. Zhang[1,]*, C. Deng[2,]*

[1]College of Material Science and Chemical Engineering, Harbin Engineering University, Harbin 150001, Heilongjiang, China; [2] Key Laboratory for Photonic and Electronic Bandgap Materials, Ministry of Education; College of Chemistry and Chemical Engineering, Harbin Normal University, Harbin, 150025, Heilongjiang, China

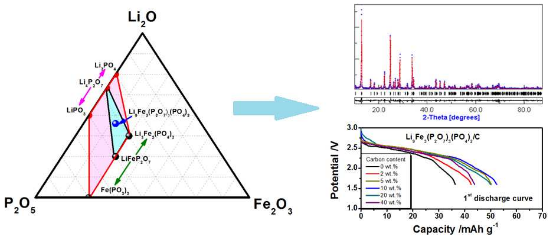

$Li_9Fe_3(P_2O_7)_3(PO_4)_2$ with mixed-polyanion groups is introduced as a novel cathode material for Li-ion batteries.